Composition−Structure−Property Relationships of 6H- and 12R-Type Hexagonal $Ba(Mn,Ti)O_{3-\delta}$ Perovskites

Laura Miranda,[†] Antonio Feteira,[‡] Derek C Sinclair,[‡] Khalid Boulahya,[†] María Hernando,[†] Julio Ramírez,[†] Aurea Varela, Jose M. González-Calbet,[†] and Marina Parras*,[†]

Departamento de Química Inorgánica, Facultad de Químicas, Universidad Complutense de Madrid, E-28040-Madrid, Spain, and Department of Engineering Materials, University of Sheffield, Mappin Street, Sheffield S1 3JD, United Kingdom

Received January 16, 2009. Revised Manuscript Received March 4, 2009

The crystal structures of 6H-type $BaMn_{0.15}Ti_{0.85}O_3$, $BaMn_{1/4}Ti_{3/4}O_{2.95}$, and $BaMn_{1/2}Ti_{1/2}O_{2.84}$ and 12R-type $BaMn_{2/3}Ti_{1/3}O_3$ have been established by a combination of X-ray, neutron, and electron diffraction, and high-resolution electron microscopy. The 6H-type structure (space group $P6_3/mmc$) can be described by a stacking sequence $(hcc)_2$ along the *c*-axis with any anion deficiency located exclusively in the h-BaO_3 layers. Ti atoms display a strong preference for the corner-shared octahedral site, whereas both Mn and Ti are distributed over the octahedral sites in the face sharing dimers. The 12R-type structure (space group $R\bar{3}m$) can be described by a stacking sequence $(hhcc)_3$. Ti atoms again display a strong preference for the isolated corner-sharing octahedral site, whereas Mn atoms occupy the central site of the face-sharing trimers. The electrical properties have been characterized by impedance spectroscopy and reveal the fully oxidized compounds to be electrical insulators with relative permittivity values of ∼45−55 at 300 K. The oxygen-deficient compounds are semiconductors, which is attributed to the presence of mixed Mn^{3+} and Mn^{4+} ions on the B-site sublattice. Antiferromagnetic (AFM) interactions occur within the face-sharing units of the respective structures. The AFM interactions inside the dimers (6H-type) and trimers (12R-type) become stronger with increasing Mn content and result in an increase in the magnitude of the Curie−Weiss constant.

Introduction

ABO_3 perovskites exhibit many useful electrical properties and for many years compounds based on B-site d^0 cations have attracted attention due to their dielectric properties, e.g., ferroelectric $BaTiO_3$, piezoelectric $Pb(Zr,Ti)O_3$, and microwave dielectric resonators based on solid solutions between two end members, e.g., $SrTiO_3$−$LaGaO_3$. In the latter case, many cubic close packed perovskites have been shown to exhibit resonance at microwave frequencies (Qf > 10 000 GHz where $Q = 1/\tan\delta$ and f is the resonance frequency) and to possess medium to high permittivity (∼25−45) with good temperature stability of the resonance frequency ($TC_f \leq \pm 30$ ppm/K).[1] Although the microwave dielectric properties of cubic close-packed perovskites have been widely studied and their structure−composition−property relationships established, much remains to be explored and understood with respect to the formation, stability and structure−property relationships of hexagonal-type perovskites.[2] Such studies may be of considerable interest for future commercial applications where higher permittivity materials (>45) are desirable.

Recently, we have been exploring $BaMn_xTi_{1-x}O_3$ compounds as they are known to contain a variety of perovskite-type phases.[3,4] The two end-members of the perovskite system $BaTiO_3$−$BaMnO_3$ have very different crystal structures at room temperature. $BaTiO_3$ is based exclusively on cubic close packed (ccp) BaO_3 layers, whereas $BaMnO_3$ is based exclusively on hexagonal close-packed (hcp) layers. The unit cell of $BaTiO_3$ at room temperature can be described as a 3C-type or $(ccc)_\infty$ structure, indicating it consists of 3 BaO_3 layers in an $(ABC)_\infty$ stacking sequence, resulting in a 3D array of corner-sharing TiO_6 octahedra. At room temperature the Ti ions are too small to occupy the centrosymmetric position within the "ideal" cubic 3C-type perovskite structure (e.g., $SrTiO_3$, $Pm\bar{3}m$); instead, they are displaced toward one of the apical oxygen ions. As a consequence, the unit cell contains a dipole moment; because of cooperative dipole interactions between adjacent unit cells, $BaTiO_3$ is ferroelectric with tetragonal symmetry ($P4mm$) and a c/a ratio of ∼1.01 at room temperature. A ferro- to paraelectric (i.e., tetragonal to cubic) polymorphic phase transition occurs at ∼403 K, above which $BaTiO_3$ attains the "ideal" 3C-type perovskite structure (up to ∼1703 K). Undoped tetragonal $BaTiO_3$ ceramics are electrically insulating (>1×10^{10} Ω cm at 300 K) and have room temperature permittivity of ∼1000−3000 (dependent on ceramic microstructure and

* Corresponding author. E-mail: mparras@quim.ucm.es. Fax: (34) 91 394 43 52.
[†] Universidad Complutense de Madrid.
[‡] University of Sheffield.

(1) Reaney, I. M.; Iddles, D. *J. Am. Ceram. Soc.* **2006**, *89*, 2063.
(2) Feteira, A.; Sarma, K.; Alford, N. Mc.; Reaney, I. M.; Sinclair, D. C. *J. Am. Ceram. Soc.* **2003**, *86*, 511.
(3) Keith, G. M.; Kirk, C. A.; Sarma, K.; Alford, N. Mc.; Cussen, E. J.; Rosseinsky, M. J.; Sinclair, D. C. *Chem. Mater.* **2004**, *16*, 2007.
(4) Keith, G. M.; Rampling, M. J.; Sarma, K.; Alford, N. Mc.; Sinclair, D. C. *J. Eur. Ceram. Soc.* **2004**, *24*, 1721.

10.1021/cm9001465 CCC: $40.75
Published on Web 04/01/2009

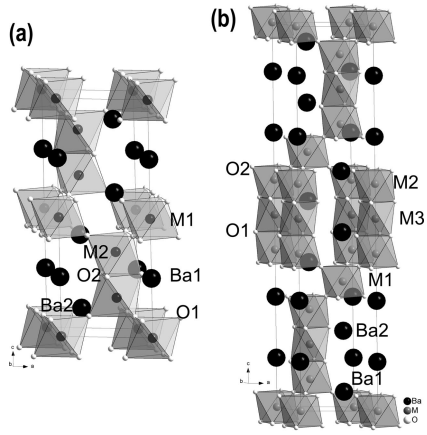

Figure 1. Structural models corresponding to (a) 6H and (b) 12R polytypes.

domain configuration).[5,6] This high permittivity coupled with the amenability of the crystal structure toward chemical doping allows the dielectric properties of $BaTiO_3$ to be engineered for a wide variety of commercial applications, such as multilayer ceramic capacitors (MLCC's).[7] The presence of ferroelectric domains, however, gives rise to higher than acceptable dielectric losses for microwave dielectric resonator applications.[8]

In contrast, the unit cell of $BaMnO_3$ can be described as 2H or $(hh)_\infty$, indicating it consists of 2 BaO_3 layers in a $(AB)_\infty$ stacking sequence, producing a structure composed of 1D chains of face-sharing MnO_6 octahedra parallel to the *c*-axis and separated by Ba^{2+} ions.[9] $BaMnO_3$ does not exhibit ferroelectricity; instead, it has a relative permittivity value of ∼15 at room temperature.[10]

The 3C- and 2H-type structures represent two extreme polytypes of the perovskite structure, i.e., 100% ccp and hcp, respectively. Numerous intermediate polytypes are known to exist, with varying degrees of mixed ccp and hcp, leading to a variety of combinations of corner- and face-sharing octahedral units. For example, undoped 3C-type $BaTiO_3$ undergoes a high-temperature polymorphic phase transition to a mixed cubic/hexagonal 6H-type structure at ∼1703−1723 K (space group $P6_3/mmc$).[11] The 6H-type cell consists of 6 BaO_3 layers in an ABCACB or $(cch)_2$ stacking sequence (66.6% ccp) and can be described as Ti_2O_9 face-sharing dimers linked by a single, corner-sharing TiO_6 unit along the *c*-axis, see Figure 1a.[9] There is metastable persistence of either polymorph in the stability region of the other in the temperature range ∼1673−1733 K;[12] however, single-phase undoped 6H-$BaTiO_3$ powders and ceramics can be stabilized in a metastable form at room temperature if quenched rapidly from ≥1748 K. Structural studies by a combination of synchrotron X-ray diffraction, neutron diffraction, and Raman spectroscopy at subambient temperatures have revealed the 6H-type cell to undergo phase transitions to an orthorhombic cell ($C222_1$) at ∼222 K and then to a monoclinic cell ($P2_1$) at ∼74 K.[13,14] Subambient dielectric data reveal anomalies associated with the phase transitions in the real and imaginary components of the complex permittivity data. The relative permittivity of undoped 6H-$BaTiO_3$ ceramics at room temperature is ∼100 and although a small dielectric anomaly is observed at ∼222 K, a large peak in permittivity (>500) at ∼74 K suggests the monoclinic form may be ferroelectric.[13] This has been confirmed by polarization−electric field measurements at low temperature. Studies on single crystals of 6H-$BaTiO_3$ revealed the anomalies in permittivity were observed only for measurements performed parallel to the *c*-axis of the unit cell. The reason(s) for 3C- to 6H-polytype transformation in undoped $BaTiO_3$ are still not fully understood and much remains to be done to understand the structure−property relationships of undoped 6H-$BaTiO_3$.

6H-$BaTiO_3$-based materials can be formed as thermodynamically stable products either by chemical doping on the Ti-site by a variety of transition metal cations,[4] e.g., Mn, Fe, Co, and Ni, and/or partial reduction of Ti^{4+} to Ti^{3+} ions[15] by annealing undoped $BaTiO_3$ in a reducing ambient at high temperature, e.g., 5% H_2 and ∼1573−1773 K. The solid solution limit for undoped, oxygen-deficient 6H-$BaTiO_{3-\delta}$ is $\delta = 0.15$. In general, both methods lead to the introduction of oxygen vacancies exclusively within the h-BaO_3 layers and, therefore, oxide ion deficiency between the face-sharing Ti_2O_9 dimers. Coulombic repulsion between the cations in the $Ti_2O_{9-\delta}$ dimers is reduced by displacement of the Ti ions away from the intervening h-$BaO_{3-\delta}$ layer, Figure 1a. Several groups have suggested the thermodynamic stability of doped or oxygen-deficient 6H-$BaTiO_3$ polytype at room temperature to be associated with the creation of oxide ion vacancies.[16,17] Other reasons, e.g., d−d orbital overlap involving d^n ($n \neq 0$ or 10) cations in the face-sharing M_2O_9 dimers, have also been suggested;[18] again, much remains to be understood regarding the thermodynamic stability of doped and/or oxygen-deficient 6H-$BaTiO_3$-based materials. Preliminary electrical studies have shown $BaTi^{4+}{}_{1-x}Ti^{3+}{}_xO_{3-\delta}$ with $\delta \geq 0.06$ to exhibit semiconductivity at room temperature and variable range (electron) hopping below room temperature associated with mixed valency on the Ti sites.[15] In contrast, dense ceramics of $BaTi_{0.95}M_{0.05}O_{3-\delta}$ (where M = Mn, Co, Fe, and Ni) are modest insulators, possess high relative permittivity (∼55−85) at room temperature, and resonate at microwave frequencies with $Qf \approx$ 1200−6000 GHz; however, the temperature stability of the resonance frequency

(5) Clark, I. J.; Marques, F. B.; Sinclair, D. C. *J. Eur. Ceram. Soc.* **2002**, *22*, 579.
(6) Arlt, G.; Hennings, D.; Dewith, G. *J. Appl. Phys.* **1985**, *58*, 1619–1625.
(7) Randall, C. A. *J. Ceram. Soc. Jpn.* **2001**, *109*, S2.
(8) Mc Neal, M. P.; Jang, S. J.; Newnham, R. E. *J. Appl. Phys.* **1998**, *83*, 3288–3297.
(9) Cussen, E. J.; Battle, P. D. *Chem. Mater.* **2000**, *12*, 831.
(10) Rawal, R. Private communication.
(11) Kirby, K. W.; Wechsler, B. A. *J. Am. Ceram. Soc.* **1991**, *74*, 1841.
(12) Akimoto, J.; Gotoh, Y.; Oosawa, Y. *Acta Crystallogr., Sect. C* **1994**, *C50*, 160.
(13) Akishige, Y.; Oomi, G.; Yamamoto, T.; Sawaguchi, E. *J. Phys. Soc. Jpn.* **1989**, *58*, 930.
(14) Noda, Y.; Akiyama, K.; Shobu, T.; Morii, Y.; Minakawa, N.; Yamaguchi, H. *J. Phys. Chem. Solids* **1999**, *60*, 1415.
(15) Sinclair, D. C.; Skakle, J. M. S.; Morrison, F. D.; Smith, R. I.; Beales, T. P. *J. Mater. Chem.* **1999**, *9*, 1327.
(16) Ahrend, H.; Kihlborg, L. *J. Am. Ceram. Soc.* **1969**, *52*, 63.
(17) Dickson, J. *J. Am. Chem. Soc.* **1959**, *81*, 4109.
(18) Dickson, J.; Katz, L.; Ward, R. *J. Am. Chem. Soc.* **1961**, *83*, 3026.

is poor[4] ($TC_f \approx 500$ ppm/K), which precludes the use of these compositions as high-permittivity microwave dielectric resonators.

In contrast to 6H-$BaTiO_3$, 2H-$BaMnO_3$ is easily reduced to become oxygen-deficient ($BaMn^{4+}_{1-x}Mn^{3+}_xO_{3-x/2}$) by heating in air at >1373 K and forms a variety of different hexagonal-type polymorphs depending on the level of oxygen deficiency. For example, with increasing temperature, Negas and Roth[19] reported that 15R- (80% hcp), 8H- (75% hcp), 6H′- (66.6% hcp), 10H- (60% hcp) and 4H-types (50% hcp) can all be formed. The structure of 6H′ is a 6-layered structure like 6H-$BaTiO_3$; however, the stacking sequence is different, (hhhchc), and this creates tetramers of face sharing Mn_4O_{15} units that are corner-linked to face-sharing Mn_2O_9 dimers.

The stacking trend in the $BaMnO_{3-\delta}$ system follows the sequence 2H → 21R-15R → 8H→6H′ → 10H → 4H,[20−24] which reveals the degree of hcp to decrease with increasing oxygen loss. The infinite 1D face-sharing strings of MO_6 octahedra in stoichiometric 2H-$BaMnO_3$ are therefore progressively replaced by shorter strings, e.g., 6H′ on partial reduction of Mn^{IV} to Mn^{III} associated with oxygen loss. Adkin and Hayward[25] have recently prepared single-phase 15R-, 8H-, 6H′-, and 10H-$BaMnO_{3-\delta}$ powders using various conditions of $T-pO_2$ and have characterized the crystal structures using neutron diffraction data. This allowed accurate location of the oxygen anions and anion vacancies to be established in this system. They showed $BaMnO_{3-\delta}$ phases to also reveal a strong preference for the anion vacancies to be located within h-BaO_3 layers as opposed to c-BaO_3 layers.

Recently, we reported the existence of a 12R-type hexagonal perovskite with composition $BaMn_{1/2}Ti_{1/2}O_3$ within the $BaTiO_3-BaMnO_3$ binary system.[3] This phase was easily prepared by a mixed-oxide route at 1523 K in air (space group $R\bar{3}m$, $a = 5.69135(2)$ Å and $c = 27.91860(15)$ Å). The structure consists of a $(hhcc)_3$ stacking sequence of BaO_3 close-packed layers along the c axis with face-sharing M_3O_{12} trimers connected by a vertex sharing octahedron, Figure 1b. Partial ordering of the Ti^{IV} and Mn^{IV} ions occurs on the B-site sublattice; Mn^{IV} ions occupy the central octahedral site in the trimers, Ti^{IV} ions occupy the octahedral site in the vertex sharing octahedra, and both ions occupy the outer octahedral site of the trimers. 12R-$BaMn_{1/2}Ti_{1/2}O_3$ is a dielectric insulator at room temperature[3] with high permittivity, $\varepsilon_r \approx 45$, $Qf \approx 12\,000$ GHz, and $TC_f = -4$ ppm/K. This showed the 12R-type compound to have much better temperature stability of the relative permittivity compared to the 6H-type $BaTi_{0.95}Mn_{0.05}O_3$.

Table 1. Experimental Conditions Used to Prepare 6H- and 12R-Type Samples

T (K)	time (h)	atmosphere
	6H-$BaMn_{1/2}Ti_{1/2}O_{2.84}$	
1273	24	air
1523	72	air
1373	72	N_2
1423	96	N_2
1473	144	N_2
	6H-$BaMn_{1/4}Ti_{3/4}O_{2.95}$	
1273	24	air
1573	96	air
1623	140	air
1648	48	N_2
	6H-$BaMn_{0.15}Ti_{0.85}O_3$	
1273	24	air
1373	96	air
1473	96	air
1523	72	air
1573	48	air
	12R-$BaMn_{1/2}Ti_{1/2}O_3$	
1273	24	air
1373	120	air
1423	48	air
1473	48	air
	12R-$BaMn_{2/3}Ti_{1/3}O_3$	
1273	24	air
1473	48	air
1648	108	air

The combination of high permittivity (>50) for 6H-$BaTi_{0.95}Mn_{0.05}O_3$ and excellent temperature stability of TC_f (−4 ppm/K) for 12R-$BaMn_{1/2}Ti_{1/2}O_3$ has led us to undertake a systematic study of the crystal chemistry, solid-solution limits, and electrical properties of 6H-$BaMn_xTi_{1-x}O_{3-\delta}$ and 12R-$BaMn_xTi_{1-x}O_3$. Here, we describe the results obtained from this study and attempt to rationalize the variations in crystal chemistry and electrical properties based on the Ti:Mn ratio and/or level of oxygen deficiency in these compounds.

Experimental Section

Powders of nominal composition $BaMn_xTi_{1-x}O_{3-\delta}$ ($0.15 \le x \le 0.67$; $0 \le \delta \le 0.16$) were prepared by the mixed oxide route from stoichiometric amounts of $BaCO_3$ (Aldrich, 99.98%), TiO_2 (Merck, 99%), and $MnCO_3$ (Aldrich, 99%). All samples were ground in an agate mortar and then transferred into alumina boats and calcined at 1273 K in air for 24 h. In all cases, stabilization of ordered single-phase compositions required long thermal treatments with repeated heating and regrinding at various temperatures, see table 1 for a summary. Three 6H-type samples were prepared, one in air ($x = 0.15$) and two ($x = 1/4$ and $1/2$) in an inert atmosphere (flowing N_2). The final heat treatment was quenched in air from 1573 K for $x = 0.15$ and slow cooling at 4 °C/min in flowing N_2 for $x = 1/4$ (from 1648 K) and for $x = 1/2$ (from 1473 K). Two 12R-type samples were prepared in air by quenching from 1473 K for $x = 1/2$ and from 1648 K for $x = 2/3$. Note that 6H-$BaMn_{1/2}Ti_{1/2}O_{3-\delta}$ was obtained by reduction of 12R-$BaMn_{1/2}Ti_{1/2}O_3$ prepared in air.

The average cationic composition was determined by X-Ray Fluorescence (XRF). The overall oxygen content was determined by thermogravimetric analysis on a thermobalance based on a CAHN D-200 electrobalance which allows determination of the oxygen content within $\pm 1 \times 10^{-3}$ on a sample of about 100 mg working under 300 mbar H_2/ 200 mbar He atmosphere.

Powder X-ray diffraction (XRD) patterns were collected using Cu Kα monochromatic radiation ($\lambda = 1.54056$ Å) at room

(19) Negas, T.; Roth, R. S. *J. Solid State Chem.* **1971**, *3*, 323.
(20) Parras, M.; Alonso, J.; González- Calbet, J. M. *Solid State Ionics* **1993**, *63−65*, 614−619.
(21) González-Calbet, J. M.; Parras, M.; Alonso, J. M.; Vallet- Regí, M. *J. Solid State Chem.* **1993**, *169*, 99.
(22) González-Calbet, J. M.; Parras, M.; Alonso, J. M.; Vallet- Regí, M. *J. Solid State Chem.* **1994**, *111*, 202–207.
(23) Parras, M.; González-Calbet, J. M.; Alonso, J.; Vallet- Regí, M. *J. Solid State Chem.* **1994**, *113*, 78–87.
(24) Parras, M.; Alonso, J.; González-Calbet, J. M.; Vallet- Regí, M. *J. Solid State Chem.* **1995**, *117*, 21–29.
(25) Adkin, J. J.; Hayward, M. A. *Chem. Mater.* **2007**, *19*, 755.

temperature on a Panalytical X'PERT PRO MPD diffractometer equipped with a germanium 111 primary beam monochromator and X'Celerator fast detector. Neutron powder diffraction (NPD) data were collected at room temperature on the high resolution powder diffractometer D2B at the Institute Laue Langevin (ILL), Grenoble, France, with neutrons of wavelength 1.594 Å. The angular range covered by the detector was 0−160° in step sizes of 0.05°. Diffraction data were analyzed by the Rietveld method[26] using the Fullprof program.[27]

Selected area electron diffraction (SAED) and high-resolution electron microscopy (HREM) were performed in a JEOL 3000 FEG electron microscope, fitted with a double tilting goniometer stage (±22 °, ± 22 °). Simulated HREM images were calculated by the multislice method using the MacTempas software package. EELS data were obtained from a Jeol 3000FEG transmission electron microscope operating at 300 kV, equipped with Enfina EELS attachment. The energy resolution was better than 1 eV for all spectra as measured by the full-width at half-maximum (fwhm) of the corresponding zero-loss peak. Both the background and plural scattering have to be subtracted from the experimental spectra to isolate the white-line intensities.

Magnetic properties were measured in a SQUID magnetometer. DC magnetization was measured in the range ∼2−320 K under an applied magnetic field of 1 kOe. AC magnetic susceptibility was measured under AC field of 2 Oe at different frequencies of 0.5, 5, 50, and 498 Hz.

Powder was milled using a mortar and pestle and uniaxially pressed (Specac, Kent, U.K.) into cylindrical 5 mm diameter pellets under an applied pressure of 50 MPa and then isostatically pressed (model CIP 32330, Flow Autoclave System Inc., Columbus, OH) at 200 MPa. Pellets were sintered for 2 h under the same atmosphere at the highest temperature of the respective powder synthesis process. An $x = 2/3$ pellet was also sintered at 1648 K for 5 h under an O_2 atmosphere with a slow cooling rate (4 °C/min). Electrodes fabricated from gold paste (T-10112, Engelhard-CLAL, Cinderford, Gloucestershire, U.K.) were applied to both faces of the pellets, which were sintered in air at 1073 K for 1 h to remove volatiles and harden the residue. Electrical properties of $BaMn_xTi_{1-x}O_{3-\delta}$ ceramics were investigated in the temperature range 8−300 K using a cryocooler coupled to an LCR bridge (model HP 4284, Hewlett-Packard, Palo Alto, CA) and to an impedance analyzer (model HP 4192A, Hewlett-Packard, Palo Alto, CA) for fixed-frequency capacitance and impedance spectroscopy measurements, respectively. The temperature range 300−800 K was measured using a ceramic jig in a high-temperature furnace coupled to impedance analyzer (model HP 4192A, Hewlett-Packard, Palo Alto, CA). All impedance data were corrected for sample geometry and analyzed using the commercial software package Z-view (Scribner Associates, Inc., Charlottesville, VA, version 2.1).

Results and Discussion

Compositional and Structural Characterization. XRD data collected from x=0.15 and 1/4 were fully indexed on the 6H-type $BaTiO_3$ hexagonal cell ($P6_3/mmc$). XRD data for $x = 1/2$ and 2/3 processed in air could be fully indexed on the 12R-type $BaMn_{1/2}Ti_{1/2}O_3$ rhombohedral cell ($R\bar{3}m$).

Hydrogen reduction TGA was carried out to determine the oxygen content of the samples. Samples were reduced to a constant weight under 300 mbar H_2/200 mbar He atmosphere and heated at 3 °C/min up to 973 K. XRD data show the final products of the reduction process to depend on the Ti/Mn ratio according to the following reduction pathways

$$\text{for } 0 \le \text{Ti} \le 0.5: \quad BaMn_xTi_{1-x}O_{3-\delta} \rightarrow (1-x)Ba_2TiO_4 + xMnO + (2x-1)BaO \quad \text{(i)}$$

$$\text{for } 0.5 \le \text{Ti} \le 1: \quad BaMn_xTi_{1-x}O_{3-\delta} \rightarrow (1-x)BaTiO_3 + x/2Ba_2MnO_3 + x/2MnO \quad \text{(ii)}$$

Under the above experimental conditions, the obtained weight loss is 1.03% for $x = 0.15$, 1.37% for $x = 1/4$, 3.38% for $x = 1/2$ (12R-sample), 2.32% for $x = 1/2$ (6H-sample), and 4.5% for $x = 2/3$. From this, the oxygen content for $x = 0.15$, 1/2 (12R-sample), and 2/3 correspond to 3 per unit formula (theoretical values of 1.025, 3.38, and 4.50, respectively), indicating that they are oxygen stoichiometric within experimental errors. In contrast, $x = 1/4$ and $x = 1/2$ (6H-sample) are anionic deficient, with compositions of $BaMn_{1/4}Ti_{3/4}O_{2.95}$ and $BaMn_{1/2}Ti_{1/2}O_{2.84}$.

An EELS study to establish the formal oxidation state of Mn in oxygen-deficient $BaMn_{1/4}Ti_{3/4}O_{2.95}$, using $BaMnO_3$ (Mn^{IV}) and $TbMnO_3$ (Mn^{III}) as internal standards. For comparison, the EELS spectra corresponding to stoichiometric $BaMn_{0.15}Ti_{0.85}O_3$ is also shown. The Mn $L_{2,3}$ edges for $BaMnO_3$, $BaMn_{0.15}Ti_{0.85}O_3$, $BaMn_{1/4}Ti_{3/4}O_{2.95}$, and $TbMnO_3$, normalized to the intensity of the L_3 maximum, are shown in Figure 2. The results show the Mn oxidation state in $BaMn_{0.15}Ti_{0.85}O_3$ to be similar to that of the $BaMnO_3$ internal standard, whereas significant differences are observed for $BaMn_{1/4}Ti_{3/4}O_{2.95}$, where an intermediate case between $BaMnO_3$ and $TbMnO_3$ internal standards is observed; the analysis of $MnL_{2,3}$ edge positions, the energy difference of the Mn(L_2-L_3) edges and the intensity ratio of the Mn(L_3/L_2) edges analysis revealed all Mn in $BaMn_{0.15}Ti_{0.85}O_3$ to be in the IV oxidation state, whereas both Mn^{IV} and Mn^{III} are present in $BaMn_{1/4}Ti_{3/4}O_{2.95}$.

Structural refinement of these oxides has been carried out using a combination of XRD and NPD data. For $x = 0.15$ and 1/4, the atomic positions corresponding to the 6H-$BaTiO_3$[28] polytype were taken as a starting model in the $P6_3/mmc$ space group. As the X-ray scattering factors and neutron scattering lengths (Ti = −3.438 fm and Mn = −3.73 fm) for these atoms are very similar, Mn and Ti were randomly distributed over the two available metal sites according to the Mn:Ti ratio. The refinements were stable and an isotropic displacement parameter for each atom was refined successfully. The O1 and O2 occupancies were also refined. In agreement with the TGA results, both sites are fully occupied for $x = 0.15$, confirming a stoichiometry of $BaMn_{0.15}Ti_{0.85}O_3$. The oxygen occupancy for $x = 1/4$ was less than unity (see Table 2); the composition from the refinements was $BaMn_{1/4}Ti_{3/4}O_{2.95}$, which is also in good agreement with the TGA analysis. The oxygen vacancies are located within the hexagonally stacked layers, which separate the pairs of face-sharing dimers, $Ba(1)O(2)_3$ in Figure 1a. Many systems including 6H-$BaTiO_{3-\delta}$[15] and $BaMnO_{3-\delta}$[25] show evidence of anionic vacancies only within the "hexagonal" stacked layers. This

(26) Rietveld, H. M. *J. Appl. Crystallogr.* **1969**, *2*, 65.
(27) Rodríguez- Carvajal, J. *J. Phys. B* **1993**, *192*, 55.
(28) Burbank, R. D.; Evans, H. T. *Acta Crystallogr.* **1948**, *1*, 330.

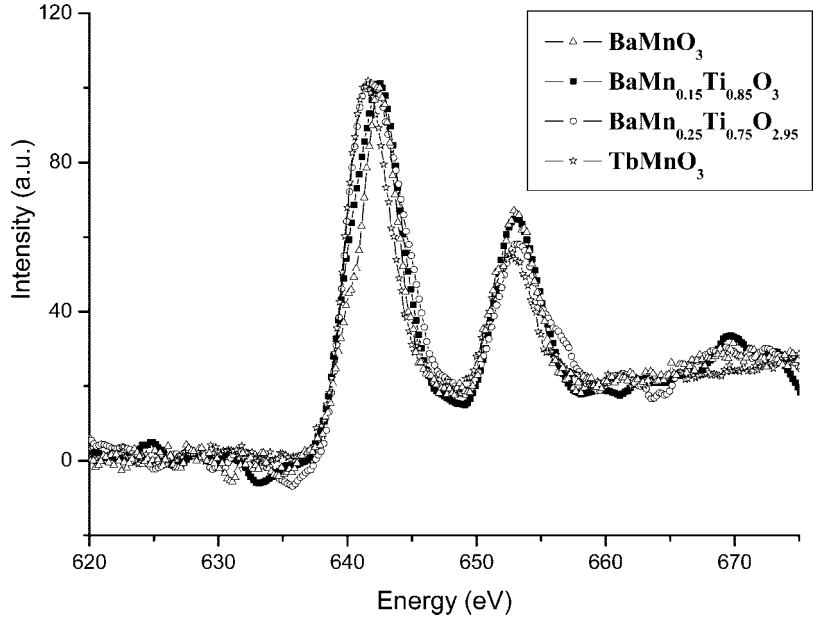

Figure 2. EELS spectra of the Mn L2,3 edges for $BaMnO_3$, $BaMn_{0.15}Ti_{0.85}O_3$, $BaMn_{1/4}Ti_{3/4}O_{2.95}$, and $TbMnO_3$. Data have been normalized to the intensity of the L3 maximum.

Table 2. Final Structural Parameters of 6H-$BaMn_{0.15}Ti_{0.85}O_3$ and 6H-$BaMn_{1/4}Ti_{3/4}O_{2.95}$[a]

		6H-$BaMn_{0.15}Ti_{0.85}O_3$	6H-$BaMn_{1/4}Ti_{3/4}O_{2.95}$
Ba(1) (0, 0, 1/4)	B_{iso} (Å^2)	0.16(4)	0.16(6)
Ba(2) (1/3, 2/3, *z*)	*z*	0.09568(10)	0.09538 (14)
	B_{iso} (Å^2)	0.28(3)	0.35(4)
M(1) (0, 0, 0)	B_{iso} (Å^2)	0.3(1)	0.7(1)
	Occ	0.15/0.85[b]	0.25/0.75[b]
M(2) (1/3, 2/3, *z*)	*z*	0.6538(2)	0.6540(3)
	B_{iso} (Å^2)	0.47(8)	0.6(1)
	Occ	0.15/0.85[b]	0.25/0.75[b]
O(1) (*x*, 2*x*, *z*)	*x*	0.8341(2)	0.8344(2)
	z	0.08036(10)	0.08074(11)
	B_{iso} (Å^2)	0.50(3)	0.63(4)
O(2) (*x*, 2*x*, 1/4)	*x*	0.5180(4)	0.5186(5)
	B_{iso} (Å^2)	0.46(4)	0.34(5)
	Occ	1	0.95(1)
a = *b* (Å)		5.70947(4)	5.71578(12)
c (Å)		13.9408(1)	13.95102(16)
V (Å^3)		393.560(4)	394.9926

[a] Space group $P6_3/mmc$. [b] Mn/Ti ratio. Metal sites occupancy cannot be distinguished from the scattering lengths. Fit parameters for XRD: $R_p = 8.66$, $R_{wp} = 10.9$, $R_B = 3.16$, $\chi^2 = 2.58$. For NPD: $R_p = 4.23$, $R_{wp} = 5.66$, $R_B = 2.28$, $\chi^2 = 2.67$.

seems to be a common feature of many hexagonal polytypes with a nonordered distribution of anionic vacancies.

Panels a and b in Figure 3 show the fitting of the XRD and ND data and the difference profile between observed and calculated data corresponding to 6H-$BaMn_{1/4}Ti_{3/4}O_{2.95}$. The refined atomic positions of both $x = 0.15$ and 1/4 6H-polytypes are listed in Table 2 and selected interatomic distances and angles are given in Table 3.

In this structure (Figure 1a), there are two crystallographically different octahedral sites, M1 and M2, that correspond to the isolated corner-sharing octahedron and the face sharing-octahedral dimer, respectively. M1 is a very regular site with six identical distances, whereas M2 has three short and three long M−O distances, Table 3. The M−M distance between the face-sharing dimers, Table 3, is close to that found in 6H-$BaTiO_3$, 2.690 Å.[12] To reduce electrostatic repulsion between the metal ions within the face-sharing units, the ions on the M2 sites are displaced from their central positions toward the adjacent cubic layer. Consequently, the face sharing dimers are distorted with three longer and three shorter M2−O distances, Table 3.

As previously mentioned, the Mn/Ti distribution over the distinct octahedral sites in these compounds cannot be refined from the diffraction data. Nevertheless, a cationic distribution for these 6H-type compounds according to the M−O distances and from bond valence sum (BVS) calculations can be proposed. BVS calculations were performed for Mn and Ti in the different M sites using bond lengths from Table 3 and are summarized in Table 4. Ti atoms display a strong preference for the corner shared octahedron (M1 site), whereas both Mn and Ti must be distributed over the octahedral dimers (M2). The M1−O distances of 1.9866(13) Å for $x = 0.15$ and 1.9896(12) Å for $x = 1/4$ are in excellent agreement with the Ti−O bond length in 6H-$BaTiO_3$ (1.983(5) Å).[15] In addition, the shorter average distance M2−O (∼1.95 Å) is in agreement with the presence of Mn atoms in this M site. From this analysis, the following cationic distributions are proposed, $Ba(Ti_{0.33})_{M1}(Ti_{0.52}Mn_{0.15})_{M2}O_3$ for $x = 0.15$ and $Ba(Ti_{0.33})_{M1}(Ti_{0.42}Mn_{0.25})_{M2}O_{2.95}$ for $x = 1/4$.

For $x = 2/3$, the 12R-polytype is stabilized, Figure 1b. The change from 6H-$(hcc)_2$ to 12R-$(cchh)_3$ polytype for higher *x* values can be attributed to the decrease in the average B cation size leading to a higher value of the tolerance factor ($t \approx 1.09$), which favors hexagonal layer stacking.

XRD and NPD data collected for $BaMn_{2/3}Ti_{1/3}O_3$ show it to be isostructural with $BaMn_{1/2}Ti_{1/2}O_3$, the 12R-$(hhcc)_3$ polytype.[3] Refinement of this structural model using the NPD data results in a good fit ($\chi^2 = 1.61$).

Figure 4 a and b show the graphical fitting of the XRD and ND data. Structural details are given in Tables 5 and 6. The refinement of the oxygen occupancy shows the anionic sublattice is complete indicating that both, Ti and Mn are

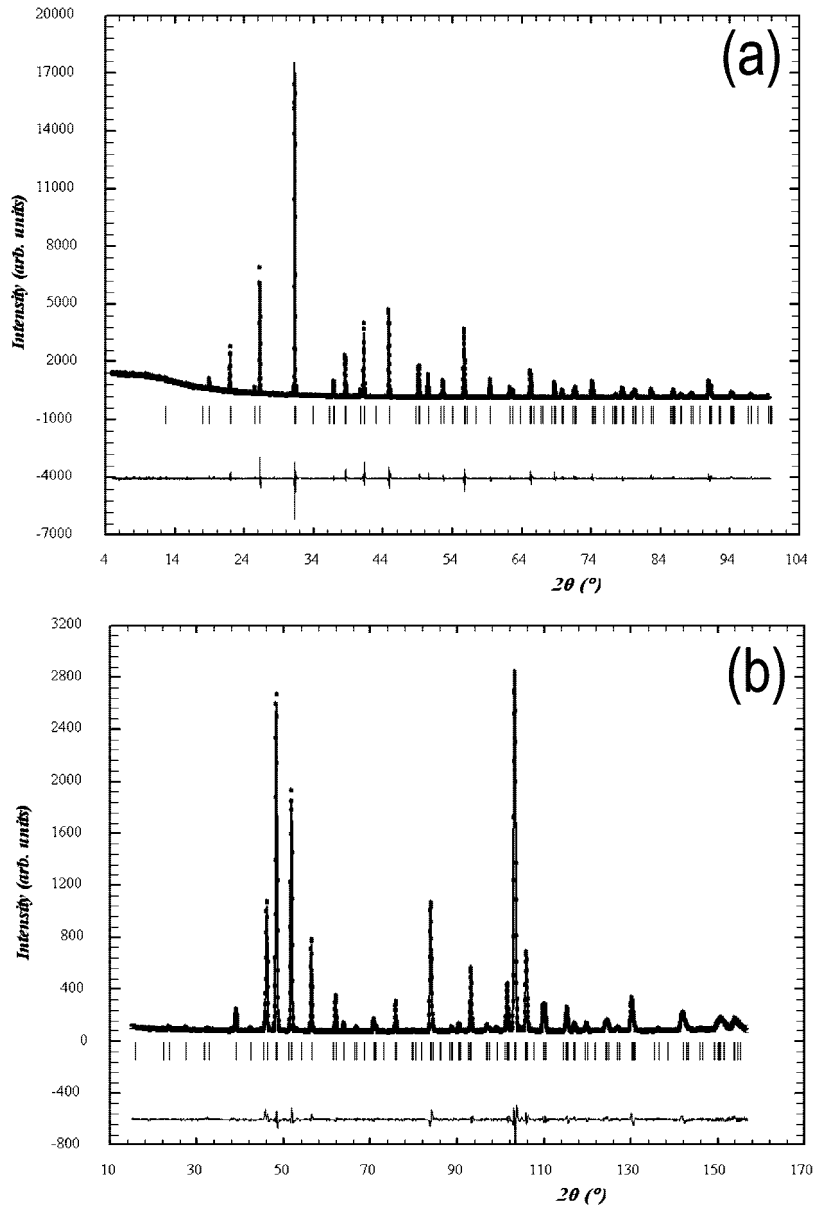

Figure 3. Observed, calculated, and difference profile (a) X-ray and (b) neutron diffraction patterns for 12R-$BaMn_{2/3}Ti_{1/3}O_3$ at room temperature.

Table 3. Selected Interatomic Distances (Å) for 6H-$BaMn_{0.15}Ti_{0.85}O_3$ and 6H-$BaMn_{1/4}Ti_{3/4}O_{2.95}$

	6H-$BaMn_{0.15}Ti_{0.85}O_3$	6H-$BaMn_{1/4}Ti_{3/4}O_{2.95}$
Ba(1)−O(1) ×6	2.8783(13)	2.8760(14)
Ba(1)−O(2) ×6	2.860(2)	2.864(3)
Ba(2)−O(1) ×6	2.8627(8)	2.8652(8)
Ba(2)−O(1) ×3	2.9605(17)	2.967(2)
Ba(2)−O(2) ×3	2.8219(17)	2.833(3)
M(1)−O(1) ×6	1.9866(13)	1.9896(12)
M(2)−O(1) ×3	1.9467(18)	1.950(2)
M(2)−O(2) ×3	1.990(3)	1.986(4)
M(2)−M(2)	2.682(4)	2.680(6)
M(1)−M(2)	3.9322(17)	3.939(2)

Table 4. Bond Valence Sums for Ti and Mn in 6H-$BaMn_{0.15}Ti_{0.85}O_3$, 6H-$BaMn_{1/4}Ti_{3/4}O_{2.95}$, and 12R-$BaMn_{2/3}Ti_{1/3}O_3$

		M1 site	M2 site	M3 site
6H-$BaMn_{0.15}Ti_{0.85}O_3$	ΣV_{Mn-O}	3.19	3.36	
	ΣV_{Ti-O}	3.77	3.97	
6H-$BaMn_{1/4}Ti_{3/4}O_{2.95}$	ΣV_{Mn-O}	3.17	3.28	
	ΣV_{Ti-O}	3.74	3.88	
12R-$BaMn_{2/3}Ti_{1/3}O_3$	ΣV_{Mn-O}	3.29	3.55	4.09
	ΣV_{Ti-O}	3.90	4.19	4.84

present in the +IV oxidation state. BVS calculations were performed for Mn and Ti in the different M sites by using bond lengths from table 6. The values obtained (see Table 4) reflect the strong preference of Mn^{4+} ions to occupy the central site of the face-sharing trimers (M3 site) whereas the isolated corner-sharing octahedron (M1 site) is fully occupied by Ti. The cationic distribution is proposed to be $Ba(Ti_{0.25})_{M1}(Ti_{0.083}Mn_{0.41})_{M2}(Mn_{0.25})_{M3}O_3$. A similar distribution has been reported[3] for 12R-$BaMn_{1/2}Ti_{1/2}O_3$.

A notable feature of the $BaMnO_{3-\delta}$ system is a change in polymorphism with δ.[19−25] This fact is also found in the Ba−Mn−Ti−O system for the $x = 1/2$ composition. Annealing 12R-$BaMn_{1/2}Ti_{1/2}O_3$ at 1473 K in flowing N_2 results in oxygen loss ($\delta \approx 0.16$) and transformation into the 6H-polytype with a composition of $BaMn_{1/2}Ti_{1/2}O_{2.84}$. In this case, the average size of the B-site cation is increased by the partial reduction of Mn^{4+} to Mn^{3+} ions. The tolerance factor therefore decreases and the 6H-

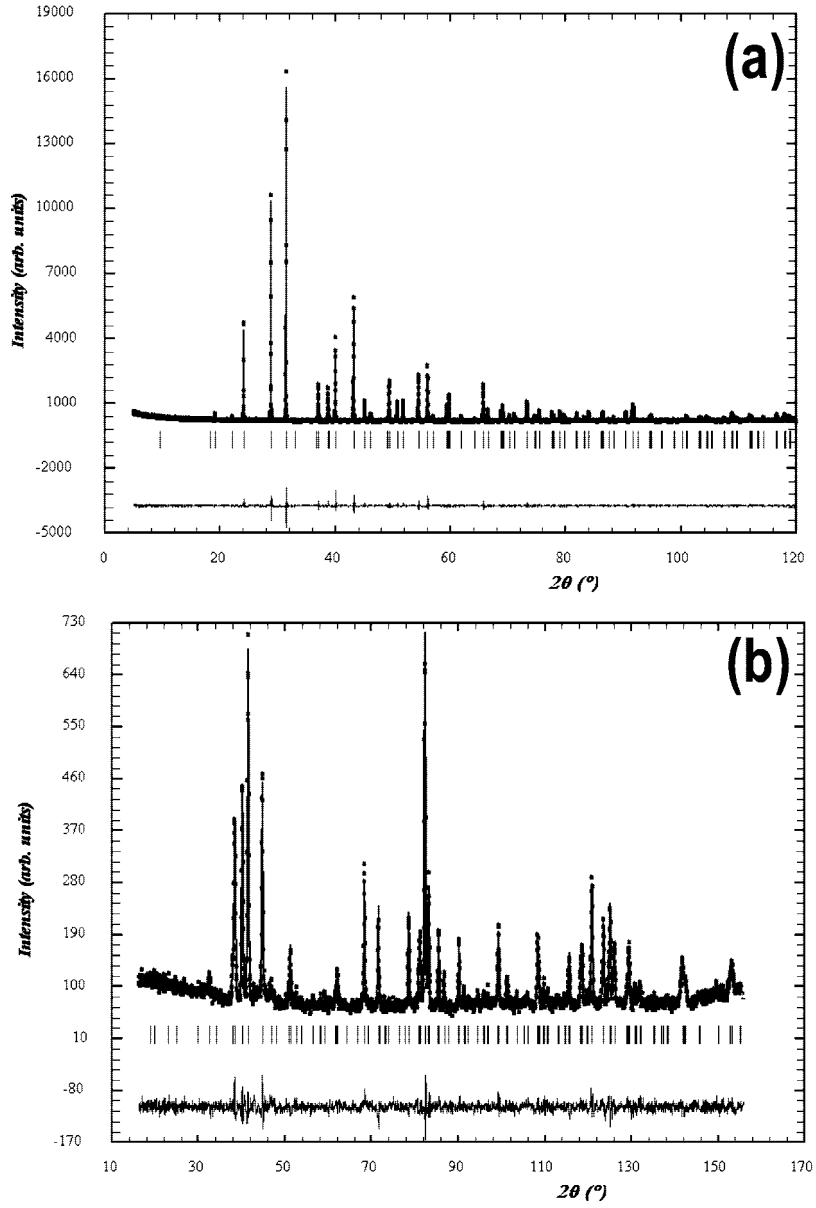

Figure 4. Observed, calculated, and difference profile (a) X-ray and (b) neutron diffraction patterns for $BaMn_{2/3}Ti_{1/3}O_3$ at room temperature.

Table 5. Final Structural Parameters Resulting from the Refinement of 12R-$BaMn_{2/3}Ti_{1/3}O_3$[a]

atoms	site	*x/a*	*y/b*	*z/c*	Occ	B_{iso} (Å^2)
Ba(1)	6c	0	0	0.28669(9)	1	0.17(5)
Ba(2)	6c	0	0	0.12807(8)	1	0.47(5)
M(1)	3a	0	0	0	0.66/0.33[b]	0.9(2)
M(2)	6c	0	0	0.4090(2)	0.66/0.33[b]	0.54(15)
M(3)	3b	0	0	0.5	0.66/0.33[b]	0.29(13)
O(1)	18 h	0.1483(6)	0.8517(6)	0.4566(2)	1	0.38(12)
O(2)	18 h	0.1681(11)	0.8319(11)	0.6264(4)	1	0.59(11)

[a] Space group $R\bar{3}m$. $a = 5.67910(2)$ Å, $c = 27.85793(16)$ Å. [b] Mn/Ti ratio. Metal sites occupancy cannot be distinguished from the scattering lengths. Fit parameters for XRD: $R_p = 6.82$, $R_{wp} = 8.96$. $R_B = 3.47$, $\chi^2 = 2.01$. For ND: $R_p = 5.87$, $R_{wp} = 7.40$, $R_B = 5.06$, $\chi^2 = 1.61$.

Table 6. Selected Interatomics Distances (Å) in 12R-$BaMn_{2/3}Ti_{1/3}O_3$

Ba(1)−O(1)	2.805(5) ×3	M(1)−O(2)	1.976(8) ×6
Ba(1)−O(2)	2.933(9) ×3		
Ba(1)−O(2)	2.845(6) ×6	M(2)−O(1)	1.970(7) ×3
		M(2)−O(2)	1.925(8) ×3
Ba(2)−O(1)	2.848(2) ×6		
Ba(2)−O(1)	2.921(5) ×3	M(3)−O(1)	1.895(5) ×6
Ba(2)−O(2)	2.936(9) ×3		
		M(3)−M(2)	2.532(6)
		M(2)−M(1)	3.899(3)

polytype (with a higher proportion of cubic layers) is stabilized. However, although this polytype appears as a single-phase by XRD, microstructural characterization shows the presence of disorder in the crystals (see below). Stacking faults are a common occurrence in polytypic materials[29−31] and are easily detected by SAED and HREM. To complete the structural studies, all samples were characterized by SAED and HREM.

SAED patterns corresponding to $BaMn_{1/4}Ti_{3/4}O_{2.95}$ along the most relevant zone axes, [010], [$1\bar{1}0$], and [001] are shown in Figure 5a−c, respectively. The data are consistent with a 6H-polytype. No sign of disorder is observed by SAED. All diffraction spots appear sharp without any apparent streaking along the *c** axis. A [010] HREM image and simulation are shown in Figure 6. In this zone, the structure is viewed parallel to the columns of Ba−O close-

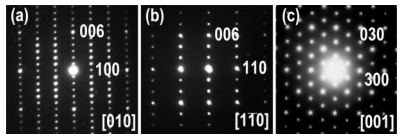

Figure 5. SAED patterns along the (a) [010], (b) [1$\bar{1}$0], and (c) [001], for $BaMn_{1/4}Ti_{3/4}O_{2.95}$.

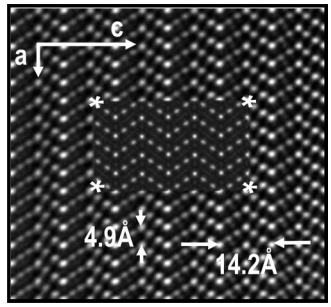

Figure 6. [010] HREM image corresponding to $BaMn_{1/4}Ti_{3/4}O_{2.95}$. The simulated image for $\Delta t = 50$ nm, $\Delta f = -540$ nm is at the inset.

packed rows and the stacking sequence of the layers is revealed directly. By consideration that Ba atoms are projected as brighter dots, the experimental contrast is associated with a (cchcch) layered sequence. This sequence extends throughout the crystal. The presence of any significant intergrowths with other polytypes can therefore be discounted. The image calculated with the atomic positions from the NPD results (inset in Figure 6) fits well with the experimental image for $\Delta t = 50$ nm, $\Delta f = -540$ nm. 6H-$BaMn_{0.15}Ti_{0.85}O_3$ shows the same ordered structure.

In contrast, 6H-$BaMn_{1/2}Ti_{1/2}O_{2.84}$ exhibits a different microstructure. SAED patterns and HREM reveal that most of the crystals show a slightly disordered microstructure. Such disorder gives rise to diffuse streaks in the SAED pattern along the [001]* direction, Figure 7a. The corresponding image shows the presence of planar faults due to intergrowths of different polytypes, Figure 7b. Two different planar distances, corresponding to 6- and 5-layer sequences, are evident along the *c*-axis. The experimental contrast variation (Figure 7c) shows the former corresponds to the $(hcc)_2$ 6H-type polymorph, whereas the obtained stacking sequence for the 5L-lamellae is (cchch), which corresponds to 1/3 of a rhombohedral 15R-polytype $(cchch)_3$, previously observed in $SrMn_{0.9}Fe_{0.1}O_3$.[29] In this case, the cubic/hexagonal layer ratio of 3/2 is in between the corresponding values for the 12R-(1/1) and 6H-(2/1) polytypes. The presence of such stacking faults can therefore be regarded as an intermediate stage of the 12R → 6H reduction process. The oxygen content was established to be 2.84 and, therefore, the relative Mn^{3+}/Mn^{4+} proportion seems insufficient to obtain an ordered, single-phase 6H polytype. Further reduction leads to decomposition of the phase with $Ba_6Mn_5O_{16}$[30] and Ba_2TiO_4[11] appearing as minority phases. It is interesting to note that the oxygen content of 2.84 is remarkably similar to the lower limited reported for reduced 6H-$BaTiO_3$.[12] The transformation of 12R to 6H via reduction may therefore be limited to the level of oxygen deficiency that can be accommodated in the 6H lattice.

Finally, SAED and HREM were used to test the extent of ordering of the 12R-polytype in the fully oxidized samples. Microstructural characterization of the $x = 1/2$ and 2/3 12R-type phases reveals differences in the microstructure of these materials. Figure 1 in the Supporting Information shows the SAED and corresponding image along [010] for 12R-$BaMn_{2/3}Ti_{1/3}O_3$. The features of both correspond to a well ordered rhombohedral $(cchh)_3$-12R polytype. For higher Ti content, $BaMn_{1/2}Ti_{1/2}O_3$, the 12R-type structure is maintained but a twinned microstructure is observed in some crystals (~65%). Figure 8 shows an SAED pattern ([1$\bar{1}$0] zone axis) for these crystals, which can be interpreted as the superposition of two domains of the 12R-type structure tilted 180° to one another around the *c*-axis. These domains are clearly visible in HREM, Figure 9. In each domain, the *d*-spacings and contrast variations are characteristics of the 12R-polytype. The optical Fourier transform of domains A and B (inset in the image) corresponds to the zone axes [010] and [0$\bar{1}$0], respectively. The inset corresponds to the FFT on the twin domain (Figure 9d) and matches with the juxtaposition of the Fourier transform of both domains, as well as the experimental SAED of Figure 8.

Magnetic Properties. The temperature dependence of the magnetic susceptibility for the 6H-$BaMn_xTi_{1-x}O_{3-\delta}$ (x = 0.15, 1/4, and 1/2) samples is shown in Figure 10. A divergence between zero-field-cooled (ZFC) and field-cooled (FC) data below ~46 K is clearly observed.

The $x = 0.15$ and 1/4 polytypes follow the Curie−Weiss law from 200 K to room temperature, Figure 10. The magnetic moment per manganese ion and the Curie−Weiss constant, obtained from fitting of the high-temperature data (in the paramagnetic range) are shown in Table 7. The negative and high value of the Curie−Weiss constant, θ, is indicative of strong antiferromagnetic interactions between the Mn cations. The effective moment calculated on the basis of Mn^{3+} and Mn^{4+} ions, both in high-spin electronic configuration, and the experimental ones ($\mu = 3.87\ \mu_B$ for $x = 0.15$ and $\mu = 4.28\ \mu_B$ for $x = 1/4$) are in good agreement with that expected from TGA, EELS and the refined compositions from NPD data. $BaMn_{1/2}Ti_{1/2}O_{2.84}$, does not exhibit Curie−Weiss behavior over the measured temperature range. This may reflect strong antiferromagnetic interactions between manganese ions within the dimers at room temperature.

12R-$BaMn_{2/3}Ti_{1/3}O_3$ does not obey the Curie−Weiss law over the measured temperature range (Figure 2 in the Supporting Information). Once again, strong antiferromagnetic interactions between the magnetic cations in the face-sharing octahedral trimers may explain this behavior. This feature is similar to that found in the isostructural 12R-$BaMn_{1/2}Ti_{1/2}O_3$, for which the large value of −350 K for θ was attributed to very strong antiferromagnetic interactions.[3] The increase in Mn/Ti ratio gives rise to a higher value of θ = −755 K.

The results show the Curie−Weiss constant to increase with the Mn content in these compounds. In 6H- and 12R-

(29) Cussen, E. J.; Sloan, J.; Vente, J. F.; Battle, P. D.; Gibb, T. C. *Inorg. Chem.* **1998**, *37*, 6071.
(30) Boulahya, K.; Parras, M.; González-Calbet, J. M.; Martínez, J. L. *Chem. Mater.* **2002**, *14*, 4006.
(31) Günter, J. R. *Acta Crystallogr., Sect. C* **1984**, *40*, 207.

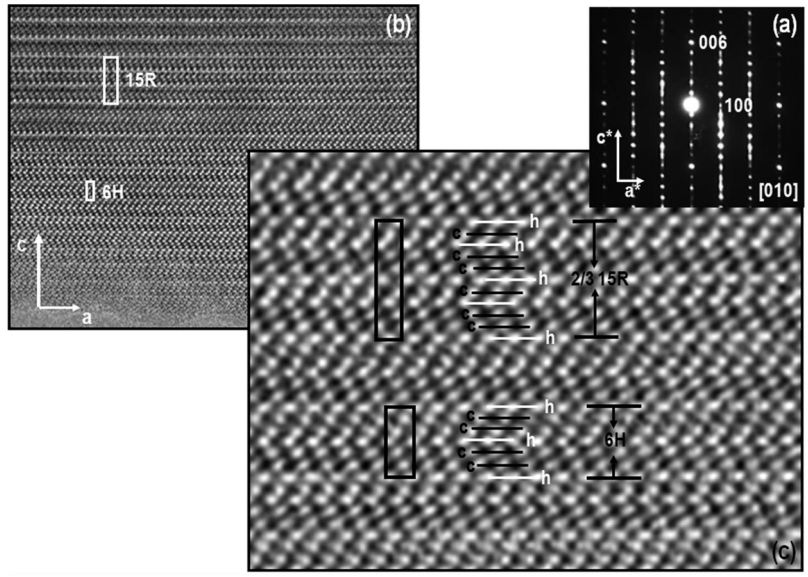

Figure 7. (a) SAED pattern along zone axis [010], (b) [010] HREM image, and (c) enlarged [010] HREM image for $BaMn_{1/2}Ti_{1/2}O_{2.84}$.

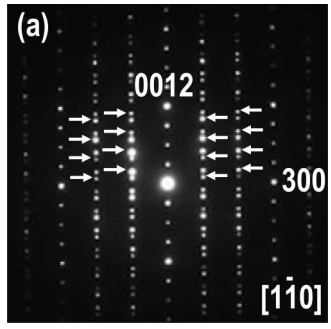

Figure 8. SAED pattern along zone axis [1$\bar{1}$0] for 12R- $BaMn_{1/2}Ti_{1/2}O_3$. The arrows show that the extra maxima correspond to the (h0l) plane.

polytypes, the M1 site associated with exclusive corner-sharing dimers is occupied exclusively by diamagnetic Ti, whereas the face-sharing dimers (6H-type) or trimers (12R-type) contain Mn ions and the remainder of the Ti content. As the Mn content increases, the antiferromagnetic interactions inside the dimers or trimers are stronger, resulting in higher absolute values of θ. The lack of long-range order in these materials may be due to the presence of the nonmagnetic TiO_6 octahedra between the dimers/trimers, because the interactions between the face sharing octahedral blocks along the *c*-axis are broken and, therefore, 3D magnetic interactions do not occur.

Finally, it is noteworthy that all samples described above show a divergence between ZFC and FC data below ~46 K. This feature has been observed previously for 12R-$BaMn_{1/2}Ti_{1/2}O_3$ where it was ascribed to the magnetic phase transition (~ 42 K) of Mn_3O_4 impurities not detectable by either XRD or NPD techniques.[3] D'Yakonov et al.[32] found the same behavior in $La_{1-x}Sr_xMn_{1+x}O_3$ perovskites, but the upward jump at low temperature was attributed to the existence of planar clusters constituted by mixed-valence Mn ions. To discriminate between these two possibilities, AC magnetic susceptibility measurements with an AC field of 2 Oe were performed at different frequencies under zero applied DC field. A broad maximum is detected around 45 K in the real component, χ', of the magnetic susceptibility data, Figure 11, in agreement with the feature observed in the DC magnetic susceptibility measurements. The temperature associated with the susceptibility maximum at ~45 K is frequency independent. This strongly supports the argument that the observed anomaly is associated with the 3D magnetic transition of Mn_3O_4 as opposed to any relaxation time process associated with planar clusters in a spin glass.

Electrical Properties. The temperature dependence of permittivity at 10 kHz for the 6H-type samples is shown in Figure 12a. Data for undoped 6H-$BaTiO_3$ are included to act as a comparison with that of the Mn-doped samples. It is clear from Figure 12a that Mn-doping has two effects on the permittivity behavior. First, the subambient phase transitions that are evident as peaks in the permittivity response of undoped 6H-$BaTiO_3$ at ~30 and 220 K and give rise to the high TC_f of this compound are suppressed on Mn doping. No peaks are observed in the permittivity response for $x = 1/4$, and this sample shows better temperature stability of the permittivity, at least below 250 K. $x = 0.15$ shows a gradual increase in permittivity on cooling but no distinct peak(s) are observed. Second, Mn doping has a dramatic effect on the magnitude of the permittivity. For example, ceramics of undoped 6H-$BaTiO_3$ and $x = 1/4$ have similar density (92 and 96%, respectively), yet the room temperature permittivity decreases from ~90 to 50. A combination of suppressing the subambient polymorphic phase transitions and partial replacement of the polarizable Ti^{4+} ions on the B-site sublattice with less polarizable cations such as Mn^{4+} and Mn^{3+} ions are the most likely reasons for the dramatic decrease in the room temperature permittivity. The permittivity of $x = 1/2$ is rather low. Although the pellet density for this ceramic was only ~88%, the dramatic decrease in permittivity cannot be attributed only to porosity. The presence of disorder in the microstructure as revealed by ED and HREM, e.g., stacking faults associated with intergrowths

(32) D'yakonov, V. P.; Pashchenko, V. P.; Zubov, É. E.; Mikhailov, V. I.; Bukhauster, Y.; Fita, I. M.; Turchenko, V. A.; Doroshenko, N. A.; Szevczik, A.; Zuberek, R.; Szymczak, G. *Phys. Solid State* **2003**, *45*, 914.

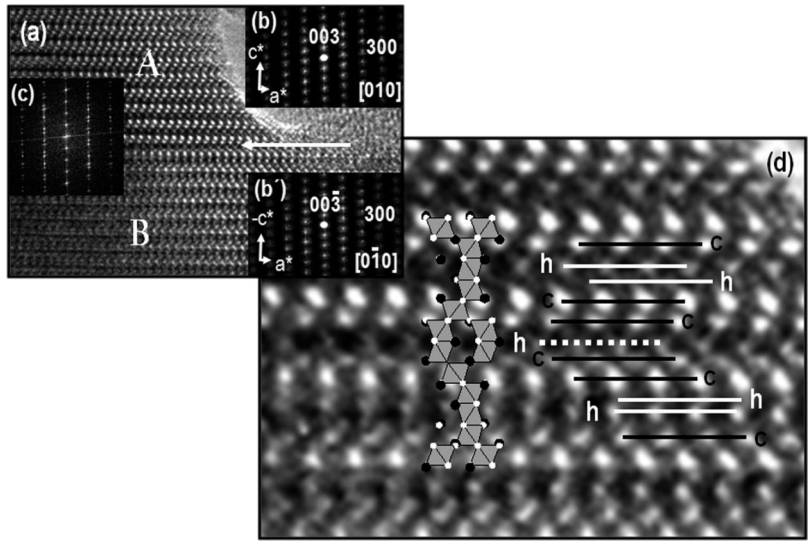

Figure 9. (a) [010] HREM image for 12R-$BaMn_{1/2}Ti_{1/2}O_3$, (b) Fourier transform (FFT) corresponding to domains marked with A and B, (c) FFT of the twin plane, and (d) enlarged HREM image with the structural model of the twin superposed and the layer sequence.

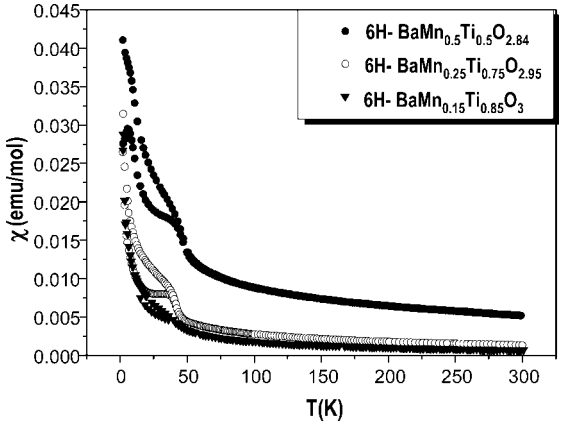

Figure 10. DC magnetic susceptibility versus temperature under an applied magnetic field of 1 kOe for $x = 0.15$, $x = 1/4$, and $x = 1/2$ 6H polytypes.

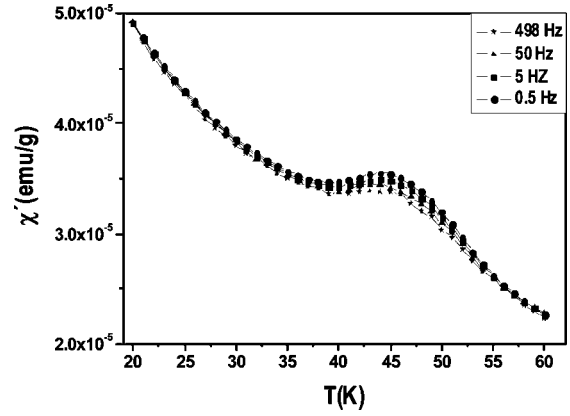

Figure 11. AC magnetic susceptibility versus temperature at different frequencies for 6H-$BaMn_{0.15}Ti_{0.85}O_3$.

Table 7. Summary of Effective Magnetic Moment, μ_{eff}, Calculated Magnetic Moment (using the spin only value), μ_{calcd}, and Curie−Weiss Constant for the Various Samples

sample	μ_{eff} (μ_B/mol)	μ_{calcd} (μ_B/mol)	θ (K)
6H-$BaMn_{0.15}Ti_{0.85}O_3$	3.75	3.87	−52.9
6H-$BaMn_{1/4}Ti_{3/4}O_{2.95}$	4.28	4.28	−122.2
6H-$BaMn_{1/2}Ti_{1/2}O_{2.84}$	4.42	3.22	−168.8
12R-$BaMn_{1/2}Ti_{1/2}O_3$[3]	4.17	3.87	−350.0
12R-$BaMn_{2/3}Ti_{1/3}O_3$	4.91	3.87	−755.0

of different polytypes seem to be the most reasonable explanation for the low permittivity.

Impedance spectroscopy data for the 6H samples showed impedance complex plane, Z^*, plots to consist of either one or two arcs, Figure 13. All data could be modeled on an equivalent circuit based on either one parallel resistor−capacitor (R,C) element (single arc in Z^* plots) or two parallel RC elements connected in series (two arcs in Z^* plots). The magnitude of the capacitance associated with the arcs was used to identify the bulk ($C < 10$ pFcm^{-1}) and grain boundary ($C > 10$ pFcm^{-1}) responses. The bulk resistivity, R_b, was estimated from the low frequency intercept of the bulk arc on the Z' axis of the Z^* plots. An Arrhenius plot showing the variation in bulk conductivity ($\sigma_b = 1/R_b$) for the 6H-type ceramics is shown in Figure 12 (b). The conductivity for all samples obeys the Arrhenius law over the measured temperature range, however, there is a significant increase in the magnitude of the conductivity and a decrease in the activation energy, E_a, associated with the bulk conduction mechanism with increasing Mn-content and oxygen-deficiency. Undoped 6H-$BaTiO_3$ and $x = 0.15$ are electrically insulating at room temperature and have $E_a \approx 0.9 - 1.0$ eV. This dielectric behavior is consistent with that reported previously for undoped and $x = 0.05$ Mn-doped ceramics[4] and confirms these samples to be fully oxidized. In contrast, $x = 1/4$ and 1/2 are examples of "leaky insulators/semiconductors" at room temperature with E_a <0.50 eV. The increase in conductivity and change in conduction mechanism is associated with the oxygen deficiency and therefore mixed valency of the Mn ions, as revealed by the results presented in the previous sections. A chemical picture of localized valencies appears more appropriate than a band model to explain the conductivity observed in $x = 1/4$ and 1/2, where electrons hop between ions by a phonon-assisted process usually referred to as polaron hopping.

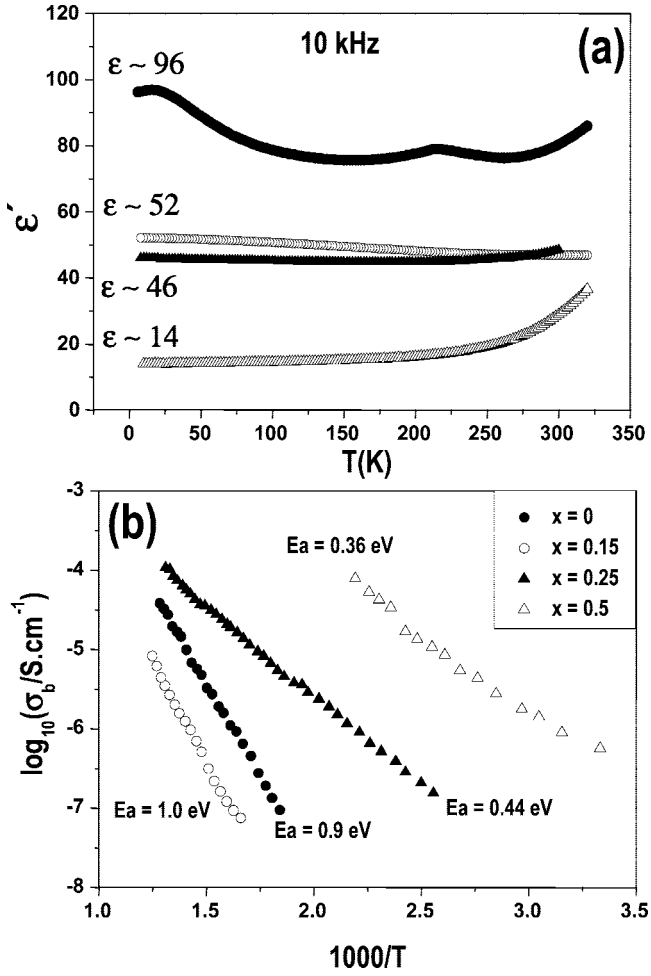

Figure 12. (a) Permittivity versus temperature and (b) Arrhenius-type bulk conductivity plots for 6H-type ceramics. Bulk activation energy, E_a, values are included in (b).

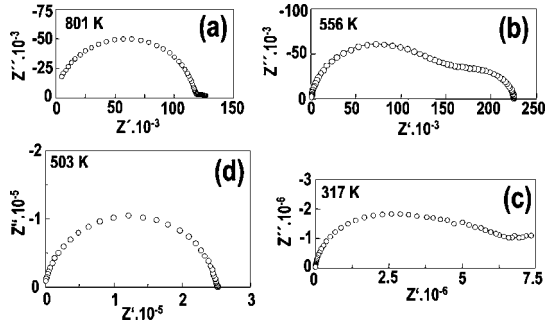

Figure 13. Z^* plots at 801, 556, 503, and 317 K for (a) $x = 0.15$, (b) $x = 0.25$, (c) $x = 0.5$, and (d) $x = 0.67$, respectively.

Similar electrical characterization was performed on the 12R-type compounds. The permittivity data reveal all 12R-type samples to exhibit an increase in permittivity with increasing temperature, Figure 14a. Increasing the Mn content again results in a decrease in permittivity. The large rise in permittivity near room temperature is an extrinsic effect associated with the "semiconducting" nature of these materials, as opposed to being an intrinsic effect. Sintering $x = 2/3$ pellets in flowing oxygen as opposed to laboratory air results in slightly higher values of permittivity and lower bulk conductivity, Figure 14b. This is consistent with previous reports for 12R-type $x = 1/2$ ceramics and is

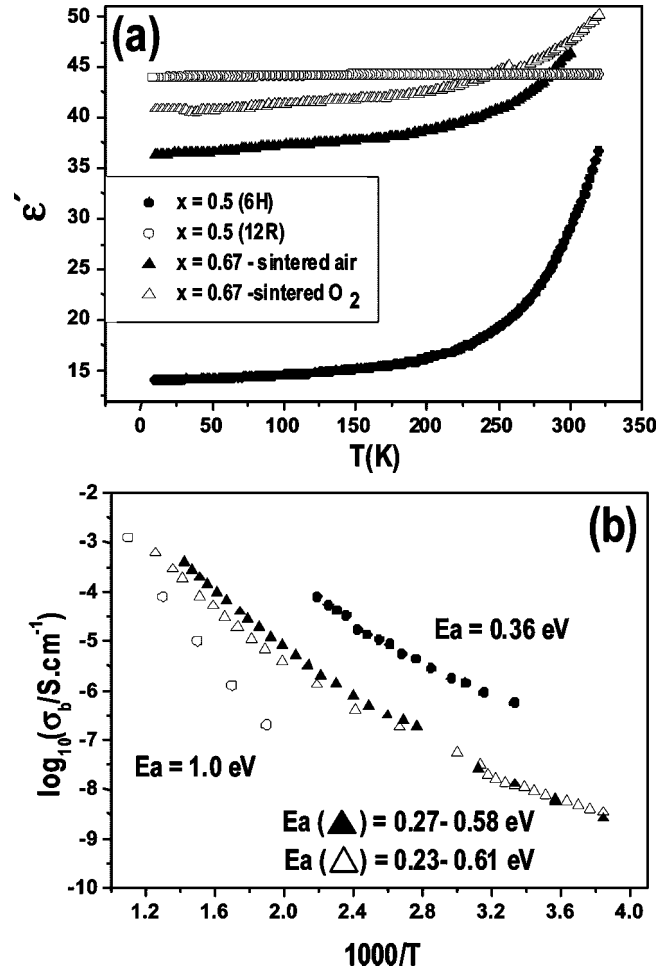

Figure 14. (a) Permittivity versus temperature and (b) Arrhenius-type bulk conductivity plots for 12R-type ceramics. Data for 6H-$BaMn_{1/2}Ti_{1/2}O_{2.84}$ are included for comparison with 12R-type $BaMn_{1/2}Ti_{1/2}O_3$. Bulk activation energy, E_a, values for the high- and low-temperature data are included in (b).

attributed to suppression of low levels of oxygen loss from samples sintered in air at elevated temperatures.[3] Although the 12R-type samples appear to be fully oxidized, non-Arrhenius-type behavior is evident for $x = 2/3$ (Figure 14b), suggesting that either a low level of oxygen deficiency and therefore mixed oxidation of Mn is present and/or a different conduction mechanism occurs in Mn-rich compositions. Data for the oxygen-deficient 6H-type $x = 1/2$ is included in Figure 14 to allow direct comparison with the fully oxidized 12R-type $x = 1/2$. The low permittivity of the 6H-type sample has been discussed above and its higher conductivity can be attributed to the significant level of mixed valency associated with the Mn ions in the 6H-type sample.

In conclusion, the structure−composition−property relationships of 6H- and 12R-type hexagonal Ba(Mn,Ti)$O_{3-\delta}$ perovskites have been established. In the case of 6H-type $x = 0.15$, the compound remains fully oxidized after ceramic processing in air and is therefore an electronic insulator with relative permittivity of ~50 at 300 K. Mn doping is effective in suppressing the subambient polymorphic phase transitions that occur in undoped 6H-$BaTiO_3$ and therefore the temperature stability of the relative permittivity of $x = 0.15$ is significantly improved compared to $x = 0$, Figure 12a. Partial replacement of Ti by Mn, however, does result in a decrease

in the magnitude of the relative permittivity. Partial reduction of Mn occurs in 6H-type $x = 1/4$ processed in an inert atmosphere (e.g., flowing N_2 at 1648 K), which results in a switch-over from insulating to semiconducting behavior, Figure 12b. The solid-solution limit for 6H-type $BaMn_xTi_{1-x}O_3$ processed in air is $x \approx 1/3$[3] but this can be extended to $x = 1/2$ by partial reduction of 12R-type $BaMn_{1/2}Ti_{1/2}O_3$ via heat treatment in an inert atmosphere, e.g., flowing N_2 at 1473 K. In all cases, Mn prefers to occupy the B-sites within the face sharing dimers, and where oxygen deficiency occurs, vacancies occur in the h-Ba(1)O(2)$_3$ layers, Figure 1a. Cation repulsion within the dimers is relieved by displacement of the B-site cations along the *c*-axis. This appears to be a general mechanism to accommodate oxygen loss from 6H-type perovskites.[3,15,25]

The 12R polytype occurs as a solid-solution phase with lower and upper limits of $x = 1/2$ and 2/3, respectively, for samples processed in air. Structural and chemical analysis suggests these samples to be fully oxidized; however, electrical characterization suggests the presence of a low level of oxygen loss. These materials can be described as leaky insulators, and again, the relative permittivity decreases with increasing Mn content, Figure 12a.

For both the 6H- and 12R-polytypes, antiferromagnetic interactions occur within the face-sharing units. As the Mn content increases, the antiferromagnetic interactions inside the dimers (6H-type) and trimers (12R-type) are stronger and therefore result in an increase in the magnitude of θ.

Acknowledgment. Financial support through research project MAT2007-61954 (Madrid), FAME-NoE FP6-500159 (Madrid, Sheffield), and EPSRC (Sheffield) is acknowledged. We thank Dra. M.T. Fernández-Díaz for assistance in collecting the neutron powder diffraction data.

Supporting Information Available: SAED pattern and HREM image along zone axis [010] for 12R-$BaMn_{2/3}Ti_{1/3}O_3$; magnetic susceptibility versus temperature under a magnetic field of 1 kOe for 12R-$BaMn_{2/3}Ti_{1/3}O_3$ (PDF). This material is available free of charge via the Internet at http://pubs.acs.org.

CM9001465